Secondary crater fields from 24 large primary craters on Mars: Insights into nearby secondary crater production

Stuart J. Robbins[1] and Brian M. Hynek[1]

Received 23 February 2011; revised 18 June 2011; accepted 15 July 2011; published 18 October 2011.

[1] Crater statistics are used across a wide variety of applications on planetary surfaces, one of the most notable being estimating relative and absolute ages of those surfaces. This requires an assumed cratering rate over time and that craters be randomly distributed. Secondary craters - craters that form from the ejecta of an impact event - belie this assumption by creating greater crater density in a local area at a single time, significantly affecting crater statistics. There has been substantial debate over the relative importance of secondary craters, and our findings in this Mars study indicate that these events can be very significant and cannot be ignored when age-dating surfaces. We have analyzed secondary crater fields found close to 24 primary craters on Mars. Among other findings such as terrain control over secondary crater field characteristics, we conclude that a single large impact event (>100 km) can significantly affect crater statistics at the ~1–5-km-diameter level over a non-trivial fraction of a planetary surface (minimum secondary crater diameters examined were ~0.9 km; the minimum primary crater diameter was ~20 km). We also suggest a potential way to avoid significant contamination by the majority of secondary craters that occur close to the primary impact event without the need to manually classify every crater as primary or secondary. Our findings are specific to Mars, but further work may show the patterns are applicable to other solid bodies.

Citation: Robbins, S. J., and B. M. Hynek (2011), Secondary crater fields from 24 large primary craters on Mars: Insights into nearby secondary crater production, *J. Geophys. Res.*, *116*, E10003, doi:10.1029/2011JE003820.

1. Introduction

[2] Crater counting on solid surfaces is the only way to estimate absolute ages on objects and regions without returned samples, akin to the Apollo missions. This common practice has been refined and utilized for decades [e.g., *Arvidson et al.*, 1979; *Hartmann*, 2005]. A fundamental assumption of crater age-dating is that crater formation is a stochastic process. However, half a century ago, *Shoemaker* [1962] identified the problem of secondary craters - craters that form from the ejecta of a larger primary impact event and are necessarily smaller than the primary. The subject of secondary craters was seldom discussed in the literature until *Bierhaus et al.* [2005] identified $>10^5$ secondary craters that contaminate crater statistics on Jupiter's moon Europa, and *McEwen et al.* [2005] identified $>10^6$ secondaries around the fresh crater Zunil on Mars; both of these studies focused on relatively small surface areas indicating large – if localized – secondary crater contamination of primary crater statistics.

[3] Understanding the role secondary craters have on local and global crater statistics is important, especially because previous research suggests that the crater population with diameters $D < 1$ km on Mars may be significantly contaminated by secondary craters [*McEwen and Bierhaus*, 2006], though in this work we show the spatial density of secondary craters may be significantly larger over broad regions of the planet. Traditionally, secondary craters are divided into two categories, the first being adjacent secondaries that typically form a distinct high-spatial density annulus of small craters around the primary, and the second being distant secondaries that are often found in clusters within rays but which also contribute to the random spatial distribution of small craters (so-called "background secondaries") [*Preblich et al.*, 2007; *Robbins and Hynek*, 2011]. Our analysis focuses on characterizing the former type because with the present and upcoming availability of high-resolution imagery of Mars, the Moon, and Mercury, detailed studies of fields of secondaries near to and far from large primary craters are becoming more important to better understand their effects on the overall crater population and hence their use and utility in discerning stratigraphy and absolute ages [e.g., *Hartmann*, 2005; *Tanaka et al.*, 2011].

[4] Using a global Mars crater database statistically complete to diameters $D = 1$ km (as measured from the overturn on a size-frequency diagram) [*Robbins*, 2011], we have identified 24 primary craters with prominent and large fields of secondary craters surrounding them (Figure 1). These craters were chosen based on examining a very high resolution version of Figure 1 and looking for apparent localized over-densities of craters in the database. While this kind of

[1]Laboratory for Atmospheric and Space Physics, University of Colorado at Boulder, Boulder, Colorado, USA.

0148-0227/11/2011JE003820

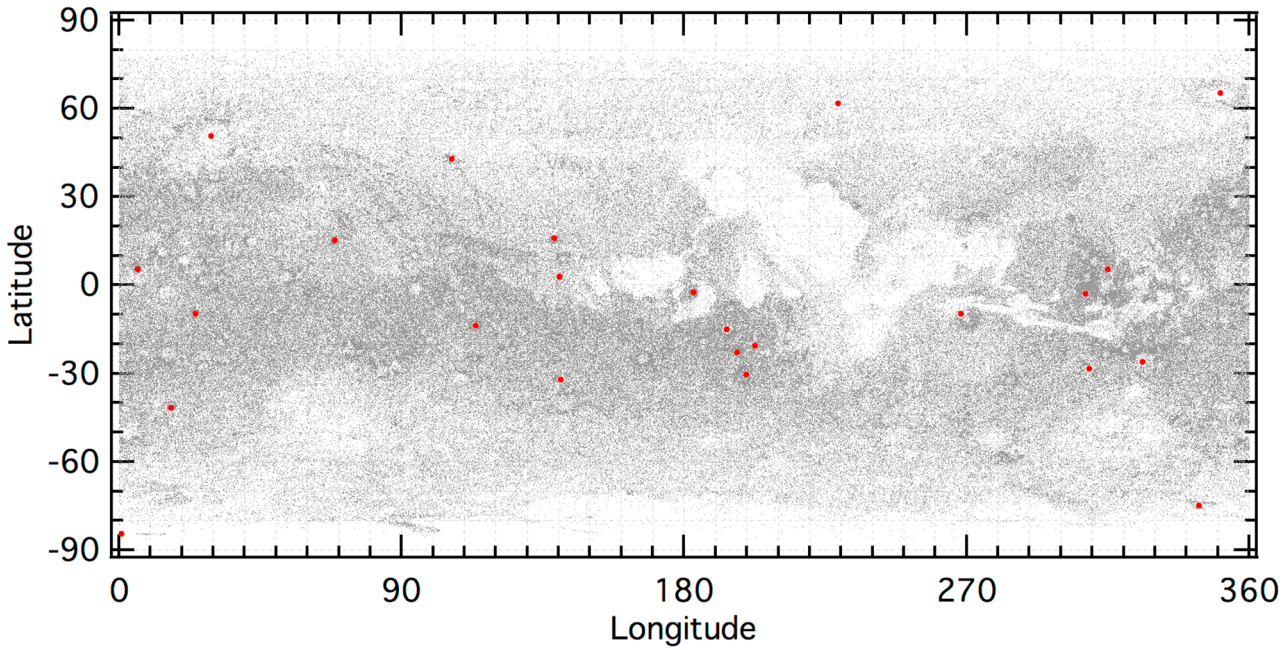

Figure 1. Distribution of all ($D \geq 0.9$ km) craters on Mars from the global Mars crater database [*Robbins*, 2011]. Each gray dot is a single crater. Red circles are the locations of all primary craters in this study.

study has been discussed briefly and theoretically in the literature [e.g., *Schultz and Singer*, 1980; *McEwen and Bierhaus*, 2006], and more studies have been conducted on very distant secondaries [e.g., *Lucchitta*, 1977; *Bierhaus et al.*, 2005; *McEwen et al.*, 2005; *Preblich et al.*, 2007; *Robbins and Hynek*, 2011], there has not been a detailed investigation of several of these nearby fields. We analyze these fields by way of number and fraction of the primary's diameter, distribution around the primary, and provide a way to account for these fields via automated methods. We discuss our methodology in identifying these craters in Section 2, explore the secondary crater field surrounding several primary craters in order of largest to smallest primary diameter in Section 3, summarize results and discuss implications in Section 4, and provide conclusions and suggest potential future investigations in Section 5.

2. Identification of Primary Craters and Their Close Secondary Craters

[5] Over 500,000 craters ≳1-km-diameter have been identified on Mars in a global Mars crater database [*Robbins*, 2011]. Craters were visually identified in ArcGIS software using 100 m/pix global THEMIS Daytime IR mosaics [*Christensen et al.*, 2004], and rims were mapped using ArcGIS's edit tools. Additional searches were made using MOLA gridded data at 1/128° scale [*Smith et al.*, 2001]. Polygons representing crater rims were imported into Igor Pro software in which a nonlinear least squares (NLLS) circle-fit algorithm was used to calculate each crater's diameter and center latitude and longitude. The NLLS algorithm corrects for map projection by converting the polygon's geographic coordinates into meters from the polygon's centroid, accounting for the first-order spherical surface of Mars. It is important to note that craters were identified regardless of morphology in this database, hence it is representative of all craters $D > 1$ km, both primary and secondary, on Mars.

[6] When identifying craters and examining the small crater distribution, numerous examples of circular-shaped over-densities of craters throughout the planet were observed (e.g., Figure 1). Further examination showed that these always surrounded a relatively large crater and, in general, most of these smaller craters had at least one morphologic characteristic that identified it as a secondary crater such as subdued topography, elongation, tightly packed clustering, or herring bone ejecta patterns [*Shoemaker*, 1962, 1965; *Oberbeck and Morrison*, 1974] (see Figures 2, 4, 5, and 6). Twenty-two such fields were selected that were from mainly pristine primary craters, clearly linked to the larger primary through trough shapes, ejecta entrainment, or axially symmetric morphologies that traced a path back to the primary (e.g., Figures 2, 4, 5, and 6); these fields were studied in greater detail (Section 3 and Table 1). A 23rd large crater was studied additionally with CTX imagery (Section 3.9) while a 24th was studied exclusively with CTX and is discussed in Section 3.10 (CTX is ConTeXt Camera from Mars Reconnaissance Orbiter [*Malin et al.*, 2007]). Care was taken to minimize contamination of these secondary crater fields with small primary craters, but there is likely inclusion at the ~1% level. The surface around primary craters was searched until morphologically distinct secondary craters were no longer found. This varied from crater-to-crater but was generally observed to be between four and six primary crater diameters.

[7] Due to the data source, this analysis is limited to craters $D \gtrsim 1$ km. While for purposes here it is assumed that these are representative of secondary craters, future, more

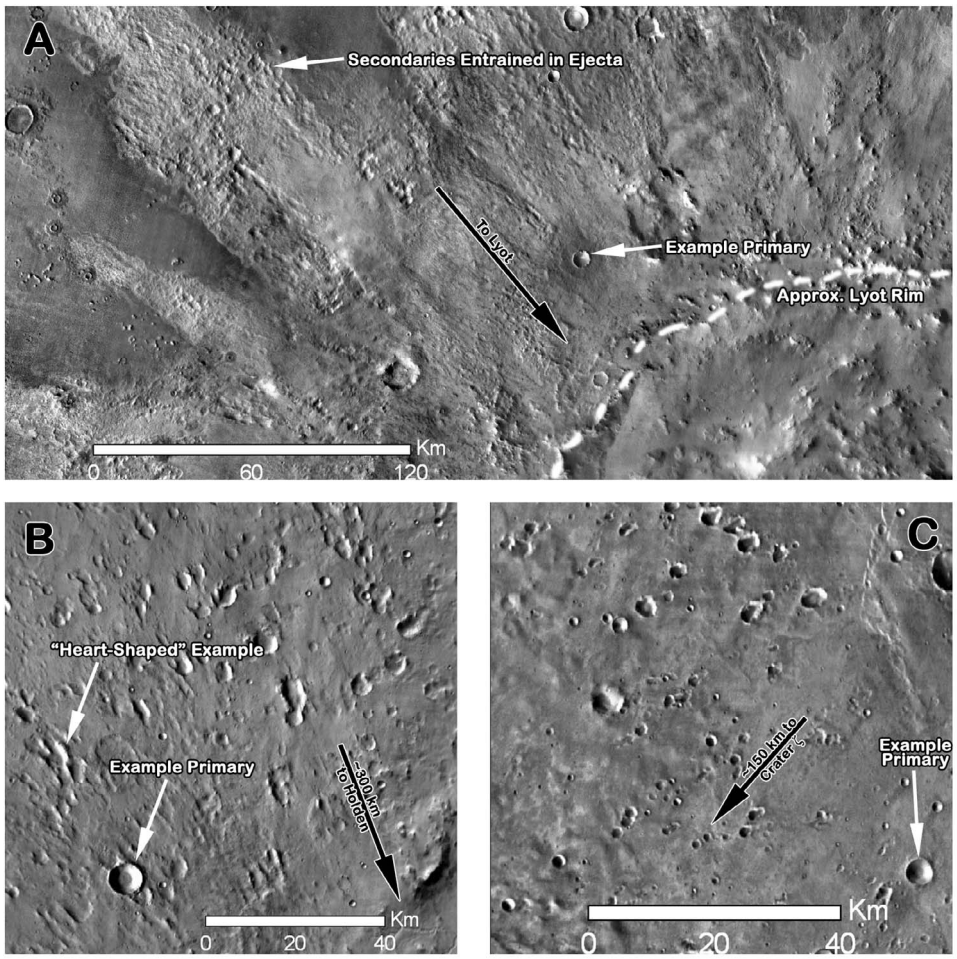

Figure 2. Examples of morphologies seen in secondary crater fields that were studied in this work. (a) Craters embedded within Lyot's ejecta and the approximate rim of Lyot. (b) Classic asymmetry, herringbone patterns, and the crater is narrower and deeper on the side facing the primary. (c) Some secondary craters display morphologies similar to primary craters with only a small amount of elongation or over-density indicating they are secondaries instead. In each frame is also marked an example of a primary crater that was of comparable size to the secondaries of interest for comparison purposes.

detailed work with orders of magnitude more craters at subkilometer sizes may find that the trends observed at kilometer scales are different. This is a limitation of our work, but the characterization of craters at kilometer sizes is important because that is generally the region in which primary craters are expected to dominate.

3. Size-Frequency Distributions of Secondary Craters

[8] Crater size-frequency distributions (SFDs) were calculated following *Arvidson et al.* [1979] with some modifications: Craters were binned in multiplicative $2^{1/8}D$ intervals for purposes of slope-fitting. Finer binning than the more standard $2^{1/2}D$ was used to bring out detail in the SFDs that would otherwise be obscured. Craters were binned such that $D_{\text{bin-1}} < D_{\text{crater}} \leq D_{\text{bin}}$, putting all craters in a diameter bin that is the largest crater size in that bin. Since the distribution of craters is not even across all diameter bins, nor does it have a single typical power law distribution with a slope of −2, the local slope between each bin and the next-smallest was used in order to shift the diameter to a more robust weighted mean:

$$D_{a'} = \frac{D_a - D_{a-1}}{1 + N(D_{a-1})/N(D_a)} + D_{a-1} \quad (1)$$

where $N(D_a)$ is the number of craters at diameter bin D_a; $D_{a'}$ is the location of diameter bin D_a after it has been shifted. This has a side-effect of having bins that are unevenly spaced in $\log(D)$.

[9] Three additional features in the SFD algorithm were run on the incremental SFDs. The first removes the largest bins with too few craters–this cut-off was set at <3 craters in a cumulative bin to eliminate some issues with small-number statistics. The second removes incremental bins that had no craters within them. The final feature removes bins below the estimated statistical completeness; this was defined as the incremental bin with the greatest number of craters. Error bars were calculated by $\pm\sqrt{N}$ Poisson statistics [*Arvidson et al.*, 1979]. Once these operations were per-

Table 1. All Primary Craters Studied in This Work With Relevant Data for Each[a]

Crater Data	Section	$N_{secondaries}$	SFD Slope	Range Fitted (km)	Annulus Parameter ($r_{primary}$)	Max. Dist. from Primary Rim ($r_{primary}$)	Terrain
50.8°N, 29.3°E, 222 km (Lyot)	3.2	2001	−5.2 ± 0.7	3.2–7.0	2.4 ± 0.9	~7	N. Plains
−26.0°N, 326.0°E, 153 km (Holden)	3.3	1541	−5.5 ± 0.7	2.7–5.9	2.3 ± 0.8	~6.5	S. High.
65.3°N, 350.7°E, 131 km (Lomonosov)	3.4	940	−8.0 ± 1.2	3.2–5.8	2.6 ± 1.1	~6	N. Plains
−9.8°N, 268.2°E, 124 km (Oudemans)	3.5	385	−6.0 ± 1.0	1.7–3.2	2.1 ± 1.3	~4	Volcanic
−14.9°N, 193.6°E, 88.6 km		563	−4.0 ± 1.5	2.7–4.9	2.3 ± 0.9	~6.5	S. High.
−2.9°N, 307.8°E, 78.8 km (Crater ζ)		508	−4.7 ± 1.0	2.1–4.5	2.0 ± 0.6	~6	Trans.
−30.3°N, 199.8°E, 77.6 km		987	−4.8 ± 0.4	1.5–4.5	2.8 ± 0.9	~6.5	S. High.
−28.4°N, 309.0°E, 77.2 km (Ritchy)		350	−4.1 ± 1.5	1.7–2.9	2.2 ± 0.6	~6	S. High.
−32.1°N, 140.8°E, 63.1 km (Horowitz)		281	−3.7 ± 0.7	1.2–3.2	2.9 ± 0.8	~5	S. High.
−13.8°N, 113.5°E, 58.5 km		123	−4.2 ± 0.7	1.2–3.2	2.3 ± 0.7	~5	S. High.
−22.7°N, 196.8°E, 55.5 km		435	−4.7 ± 1.5	1.7–2.9	2.1 ± 0.7	~6	S. High.
−9.7°N, 24.4°E, 51.4 km		213	−3.3 ± 0.7	1.3–3.5	1.9 ± 0.6	~4	S. High.
15.2°N, 68.8°E, 47.1 km		259	−4.2 ± 0.7	1.1–3.0	1.9 ± 0.8	~4.5	S. High.
42.8°N, 106.1°E, 46.3 km (Nier)		187	−6.9 ± 1.7	1.3–2.1	3.1 ± 1.3	~6	Volcanic[b]
5.3°N, 5.8°E, 45.0 km (Crater α)	3.6	174	−4.3 ± 1.3	2.3–4.7	2.2 ± 0.6	~4	S. High.
−41.7°N, 16.5°E, 41.9 km		280	−5.5 ± 1.1	1.2–2.2	1.7 ± 0.6	~5.5	S. High.
15.9°N, 138.6°E, 37.1 km		256	−5.0 ± 1.9	1.3–2.1	3.0 ± 1.0	~5	Volcanic
−2.4°N, 183.0°E, 36.3 km (Crater β)	3.7	596	−7.9 ± 2.3	1.5–2.3	1.8 ± 0.7	~6	M.F.F.
−20.6°N, 202.5°E, 34.4 km		153	−4.5 ± 1.4	1.3–2.5	2.1 ± 1.5	~5	S. High.
−74.8°N, 343.9°E, 30.4 km (Crater ε)		250	−3.8 ± 0.4	1.1–2.4	3.3 ± 1.0	~8	Polar
3.0°N, 140.3°E, 29.4 km (Crater γ)	3.8	239	−4.0 ± 0.5	1.5–3.2	2.9 ± 0.8	~5.5	M.F.F.
5.4°N, 314.9°E, 25.3 km		122	−4.7 ± 0.9	1.0–1.7	2.5 ± 0.5	~5	Trans.
−84.4°N, 0.5°E, 24.2 km (McMurdo)	3.9	217[c]	−5.2 ± 1.4	1.1–2.1	3.4 ± 1.0	~6	Pole
61.7°N, 229.0°E, 19.3 km (Crater δ)	3.10	1915[c]	−6.6 ± 1.0	0.4–0.8	5.5 ± 1.6	~10	Volcanic

[a]Craters are listed in the order of decreasing primary diameter. "Section" is the section of the text, if present, that discusses the primary crater and its associated secondary field in more detail. "SFD Slope"±values are statistical uncertainties in the fitted slopes. "Annulus Parameters" are $\mu \pm \sigma$ of fitted Gaussian from binning in units of 10% the primary crater radius. "Max. Dist. from Primary Rim" is the maximum distance (rounded to $0.5r_{primary}$) at which secondary craters were found from the primary crater. "Terrain" is a broad terrain classification into one of six categories: Volcanic, S. High. (Southern Highlands), Trans. (transitional between volcanic and southern highlands), N. Plain (Northern Plains), M.F.F. (Medusae Fossae Formation), and Pole/Polar (very near or embedded in a polar cap).

[b]The Utopia Basin is assumed to be volcanic for this purpose [e.g., *Thomson and Head*, 2001].

[c]This crater's secondary field was exclusively analyzed with CTX data.

formed, the incremental SFDs were integrated (discretely summed) to yield a cumulative SFD. Comparative R-plots (Figures 3 and 7) were calculated [*Arvidson et al.*, 1979] with similar adjustments. All slopes quoted in this paper are the slopes to NLLS of a line of the $\log_{10}$ of incremental SFDs with −1 added to yield a statistically accurate slope on a cumulative SFD [*Chapman and Haefner*, 1967]. All uncertainties in the slopes include the statistical uncertainties discussed above; without them, the uncertainties on the slopes are significantly smaller (~10% those quoted).

[10] Fifteen of the primary craters analyzed were generally similar to each other and non-unique in regards to this study, and these results are reported in Table 1 and discussed in Section 3.1. The remainder have unique context and/or properties that bear further discussion, and these are addressed in the remainder of this section.

3.1. Summary of Fifteen Similar Craters' Secondary Crater Fields

[11] Secondary crater fields were examined and analyzed in several ways: Number of secondary craters, slope of the craters on an incremental size-frequency diagram, and the averaged radial distribution of secondary craters from the primary crater. Of the 24 craters examined, fifteen were fairly similar to each other (see Table 1) and had non-unique contexts so they are not reported individually below. In general, these primary craters had a few hundred secondary craters $D \gtrsim 1$ km. Their SFD slopes were between about −3.5 and −5.0, and the secondary craters were found as far as 5–6 primary crater radii from the primary crater. The radial distribution of secondary craters closely followed a Gaussian, and the mean of the Gaussian was approximately 2.4 primary crater radii from the primary crater's rim (standard deviations were ~0.9). These could be considered a baseline from which many of the primary craters in the following sections deviated in one or more characteristics.

3.2. Lyot Crater

[12] Lyot crater is a 222-km-diameter fresh peak-ring crater located at 50.8°N, 29.3°E. It is one of the largest relatively young craters on the planet, having been dated to a Middle Amazonian age of ~1.6–3.3 Ga [*Tanaka et al.*, 2005; *Dickson et al.*, 2009]. This crater and its distant secondary crater population are discussed in-depth by *Robbins and Hynek* [2011], and this work looks more closely at the "nearby" secondary field, so-called in that work to differentiate it from secondary craters found up to 5200 km from Lyot. Lyot's secondary craters are found as close as on Lyot's rim, and the near craters that still display clear secondary morphologies (Figure 2) extend up to ~7 crater radii from the rim (750 km). The largest crater with secondary-type morphology is a $D = 28$ km crater located just outside the northwest rim, though this would be abnormally large at 13% the primary's diameter. The largest alternative is an 11-km crater to the northwest which fits the canonical 5% of primary size relation [*Melosh*, 1989].

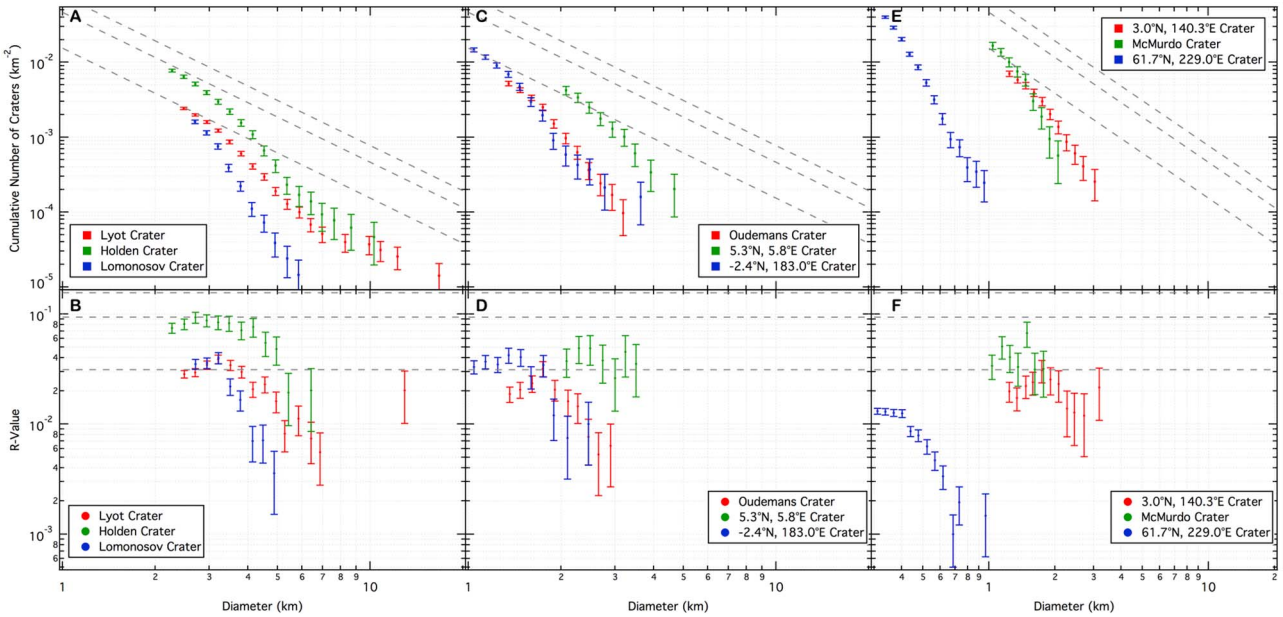

Figure 3. Cumulative (top) size-frequency distributions and (bottom) R-plots (bottom row) of all secondary crater fields discussed in Section 3. The craters in the (a, b) first three subsections, (c, d) next three, and (e, f) final three are shown. All vertical axes are the same in Figure 3, top, and they are also the same in Figure 3, bottom. The horizontal axes are the same Figures 3a–3d but differ for Figures 3e–3f. Dashed lines show 1%, 3%, and 5% of geometric saturation (geometric saturation is defined as $1.54D^{-2}$ [*Melosh*, 1989]).

[13] Morphologically, Lyot's secondary craters are clear to identify: Long, deep, radial troughs extend from Lyot up to ~300 km from the crater rim, and within them are numerous craters. These craters are generally not circular but are either amorphous in shape or biaxially symmetric with the axis of symmetry tracing back to Lyot; in many cases, they look heart-shaped (Figures 2a and 2b). The noncircular shape is generally attributed to the crater being formed under a lower impact energy [*Melosh*, 1989], and the preferential direction is due to the clear directional component of the secondary impactor's velocity. Farther from Lyot, the secondary craters are no longer entrained within troughs nor emplaced on Lyot's continuous ejecta blanket. Instead, the crater shapes point back toward Lyot and still occur in clusters, but these morphologic clues are less clear the farther from Lyot. Even farther, as discussed by *Robbins and Hynek* [2011], the secondary craters display a general lack of classic secondary characteristics and are instead identified mainly from clustering properties.

[14] 2001 nearby secondary craters from the database were extracted for Lyot, a 15% increase from *Robbins and Hynek* [2011] due to further searching (Table 1). They are generally found in an annulus around Lyot though this is not obvious until a histogram of distances from the crater center is created; the mean distance is 2.4 crater radii from Lyot's rim (270 km). When plotted in a size-frequency diagram (Figure 3a), the diameter range $3.2 \leq D \leq 7.0$ km has a slope of -5.4 ± 0.7. This is significantly steeper than a typical crater population with a slope between −2 and −3, but it is typical for secondary crater populations [*McEwen and Bierhaus*, 2006]; it was also generally typical for the other fields studied in this work, though a range of slopes were observed (see Table 1 and Section 4 for implications).

3.3. Holden Crater

[15] Holden Crater is a large, 153-km-diameter flat-floored crater located at −26.0°N, 307.8°E. It is one of the most morphologically degraded craters in this study, and it has been dated to the Noachian epoch (≥3.7 Ga) [*Scott and Tanaka*, 1986]. This crater is of special interest due to the Uzboi Vallis channel that flows into its southwest side, the presence of lake deposits and other aqueous features [*Grant et al.*, 2008], and it is a finalist landing site candidate for the *Curiosity* lander [*Golombek et al.*, 2010].

[16] Holden's secondary craters are morphologically distinct from primary craters, for they almost exclusively fall into the class of highly elliptical craters with the major axis pointed radially from Holden and the distant end having little to no rim (Figure 2b). The vast majority of the secondaries identified are $D > 1$ km, dominating the cratering statistics over a large area, at least to the north. The secondary crater distribution around Holden is almost completely to the north of the crater; this is likely due to significant resurfacing on the southern half [*Scott and Tanaka*, 1986].

[17] 1541 craters that are probable secondaries from Holden up to ~6.5 crater radii were identified from the database (Table 1). The annulus of secondaries is extensive and, when binned, the greatest density is 2.3 crater radii from the rim (172 km), though azimuthal symmetry was assumed in determining this value, ignoring erosion. The size-frequency distribution (Figure 3a) of the secondaries has a -5.5 ± 0.7 slope when fitted at diameters $2.7 < D < 5.9$ km.

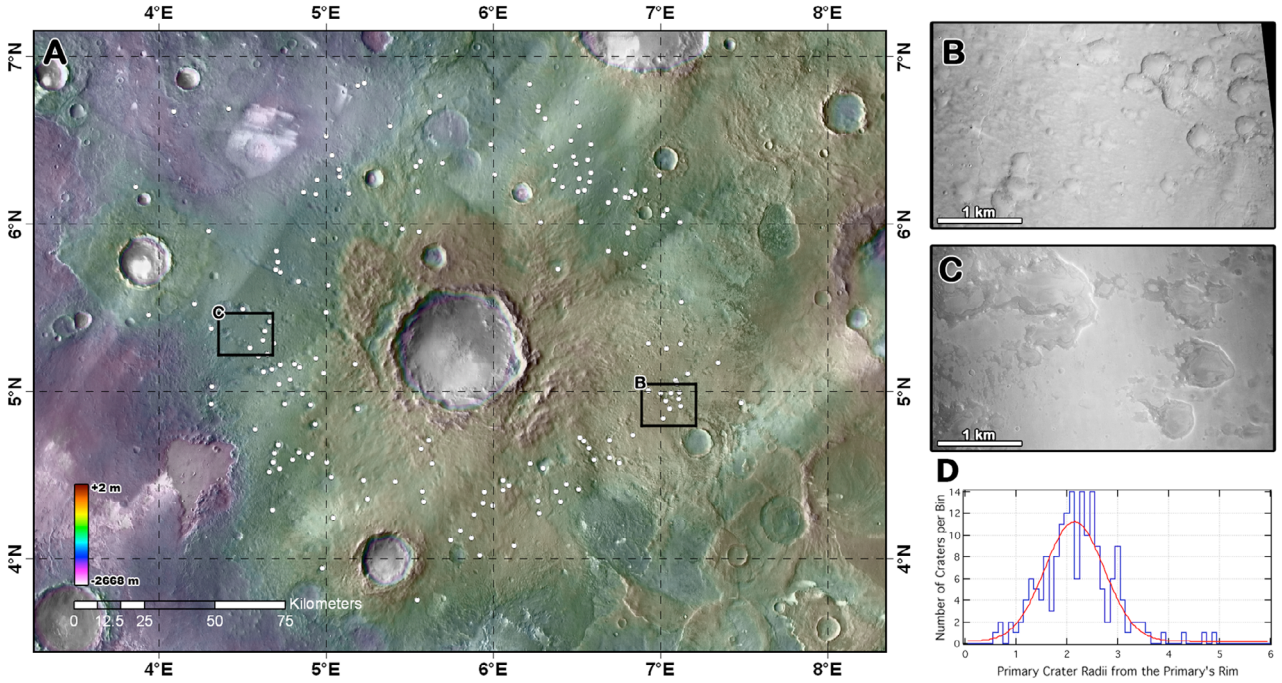

Figure 4. (a) THEMIS mosaic of Crater α located at 5.3°N, 5.8°E showing the crater and its field of nearby secondary craters (white circles). MOLA topography data [*Smith et al.*, 2001] underlies the THEMIS data. (b, c) Close-up panels are CTX data and show representative examples of the rather large secondary craters for this primary. (d) All secondaries identified show a Gaussian distribution from the crater and though they display fewer of the morphological characteristics typical of secondary craters, their relationship to the primary indicates they are indeed secondaries, despite being up to 10% the diameter of the primary.

3.4. Lomonosov Crater

[18] Lomonosov Crater is a fairly fresh central peaked 131-km-diameter crater located at 65.3°N, 350.7°E. 940 craters that are probable secondaries were extracted from up to ~6 crater radii from the rim (Table 1). They are all found in a tight annulus of ejecta with the greatest density 2.6 crater radii from the rim (170 km). The size-frequency distribution of Lomonosov's secondaries has a well-defined slope along $3.2 < D < 5.8$ km of -8.0 ± 1.2 (Figure 3a). This is the steepest slope found of the craters in this work, although the reason is not clear. One hypothesis is that it could - at least in part - be due to observational biases since large craters were preferentially not selected as potential secondaries. The problem with this hypothesis is twofold, however. First, this should affect larger diameters more than smaller, but a uniform slope over the range fit belies that. Second, Lyot crater is nearly twice as large so this effect should be compounded, but a very stable −5.4 slope for Lyot was calculated, and a similar −5.5 for Holden's secondaries was also determined. An alternative hypothesis stems from the fact Lomonosov is the furthest north crater studied and it is well within the region of the Martian cryosphere [*Boynton et al.*, 2002]. If this crater formed when the cryosphere at that latitude was in place, one may expect fewer large craters to be produced from a likely weaker near-surface crust - a crust that may more easily fragment once the released impact energy vaporizes any solid volatiles holding fragments together. A relatively steep slope for the other high-northern crater studied (Crater δ; see Section 3.10) supports this interpretation.

3.5. Oudemans Crater

[19] The eroded 124-km-diameter Oudemans Crater is a central-peaked crater located at −9.8°N, 268.2°E. The secondary craters from Oudemans are difficult to measure. The crater itself is crosscut to the north by the western parts of the vast Valles Marineris canyon system, specifically Noctis Labyrinthus and Ius Chasma. This indicates that the crater pre-dates this section of Valles Marineris, which has been estimated to be Early Hesperian, ~3.5 Ga [*Tanaka*, 1986]. Valles Marineris also obscures the northern third of the secondaries from Oudemans, and the remaining secondaries have a highly modified morphology and are difficult to identify. Nonetheless, identification of secondary craters from Oudemans was possible due to their non-circular nature and tendency to reside in lines radial to the primary.

[20] 385 craters from the database are probable secondaries from Oudemans and extend up to ~4 crater radii from the rim (Table 1); this is the smallest field in extent in this study and it is likely the field was once larger, but it is now obscured by Valles Marineris and volcanic burial. They are all found in a relatively tight annulus of ejecta with the greatest density 2.1 crater radii from the rim (130 km), though azimuthal symmetry was assumed in determining this value, ignoring erosion. The size-frequency distribution of the secondaries has a -6.0 ± 1.0 slope when fitted at $1.7 < D < 3.2$ km (Figure 3c).

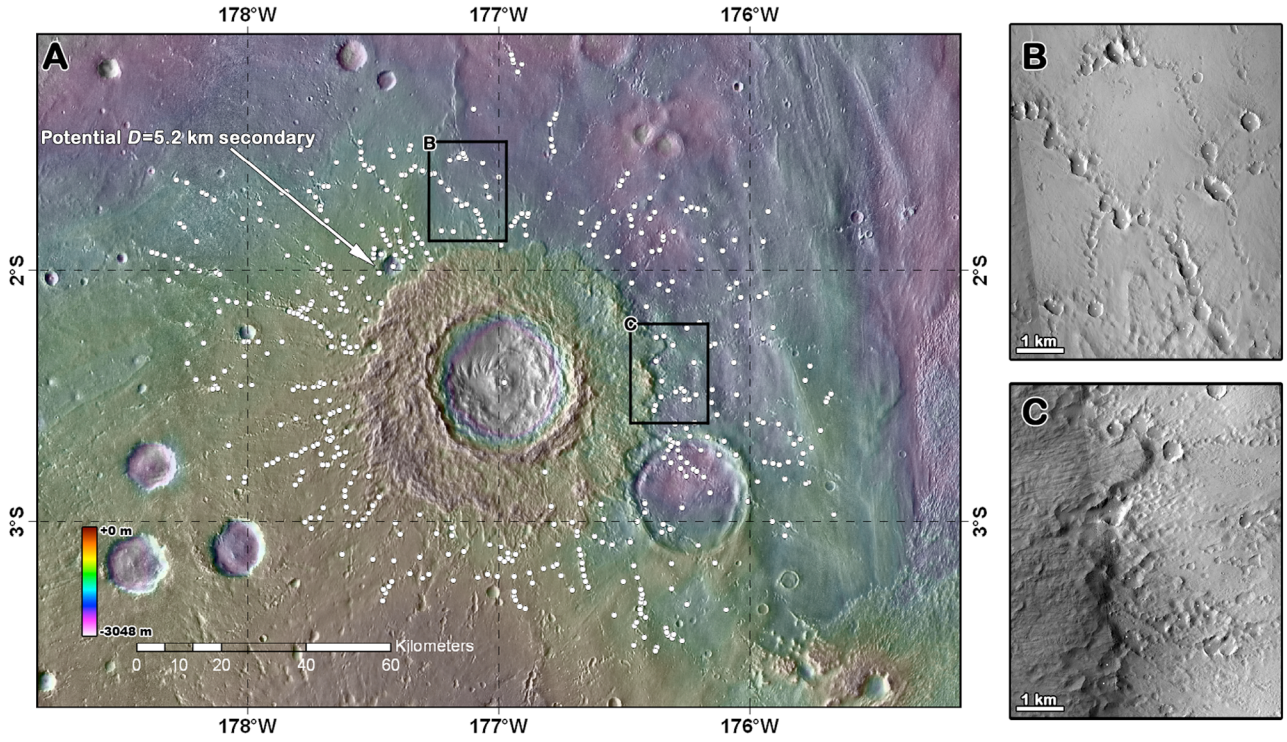

Figure 5. (a) THEMIS mosaic of Crater β located at −2.4°N, 183.0°E showing the crater, its layered ejecta blanket, and a few of the "tendrils" of secondary craters observed (secondary craters identified are white circles). MOLA topography data [*Smith et al.*, 2001] underlies the THEMIS data. (b, c) Close-up panels are CTX data and show representative examples of these tendrils (Figure 5b) and an example of some of the few secondary craters not found within them that generally abut the ejecta (Figure 5c).

3.6. Unnamed Crater at 5.3°N, 5.8°E ("Crater α")

[21] The 45.0-km-diameter crater located at 5.3°N, 5.8°E is shown in Figure 4a (and named "Crater α" in this paper). 174 craters from the database are probable secondaries from this crater that extend up to ~4 crater radii from the rim (Table 1). The greatest density is 2.2 crater radii from the rim (48 km). The size-frequency distribution of the secondaries has a -4.3 ± 1.3 slope when fitted at $2.3 < D < 4.7$ km (5.1–10.4% the primary crater diameter) (Figure 3c). This represents one of only two cases where all secondary craters from a primary in this work are larger than 5% of the primary size. However, as shown in Figures 4b and 4c, these are morphologically secondary craters, and their relationship with the primary (Figures 4a and 4d) is in concordance with the distribution expected of secondary craters.

3.7. Unnamed Crater at −2.4°N, 183.0°E ("Crater β")

[22] A broad context view of the unnamed 36.3-km-diameter fresh central peak crater located at −2.4°N, 183.0°E is shown in Figure 5a (and named "Crater β" in this paper). There is a potentially large secondary crater located 38 km from the crater's center (indicated in Figure 5a), though it is abnormally large at D = 5.2 km, 14% the diameter of the primary (similar to the larger candidate for Lyot, Section 3.2). One may expect the largest secondary to be ~1.8 km in diameter [*Melosh*, 1989], but since there are over a dozen craters approximately this size that are included in the secondary field, an alternative "largest secondary" is difficult to discern from the others.

[23] This crater and its associated secondary field presented an interesting and unique morphology among the ones studied in this work, only matched in part by the one in Section 3.10. It is one of the "layered ejecta" craters [*Barlow et al.*, 2000] characterized by a highly cohesive ejecta blanket, though this blanket also appears to have classic radial ejecta overlaying it. There are very few secondary craters upon the cohesive ejecta, which extends an average of 0.95 crater radii from the rim. Due to the lack of emplaced secondary craters, it is likely the layered ejecta blanket formed after emplacement of the secondary craters, burying any that formed closer in. Beyond the ejecta, however, are numerous tendril-like features that are chains of secondary craters (Figure 5b). Very few secondary craters were identified that were not in these thin, nonlinear chains; ones that were not in these were generally just outside the terminus of the layered ejecta blanket (Figure 5c) or they were very small and only visible in higher-resolution data. Overall, the secondary craters from this primary were also among the most deformed, being far from circular, though still morphologically fresh.

[24] 596 craters were extracted as probable secondaries from this crater at distances up to ~6 crater radii from the rim (Table 1). Though residing in the chains and tendrils, when binned they have a peak mean distance of 1.8 crater radii from the crater's rim (33 km). This was a unique case among the crater fields studied where a lognormal distribution better-represented the radial distribution of secondary craters from the primary, which had a mean of 1.6 crater radii; this is likely an artifact of the ejecta blanket covering

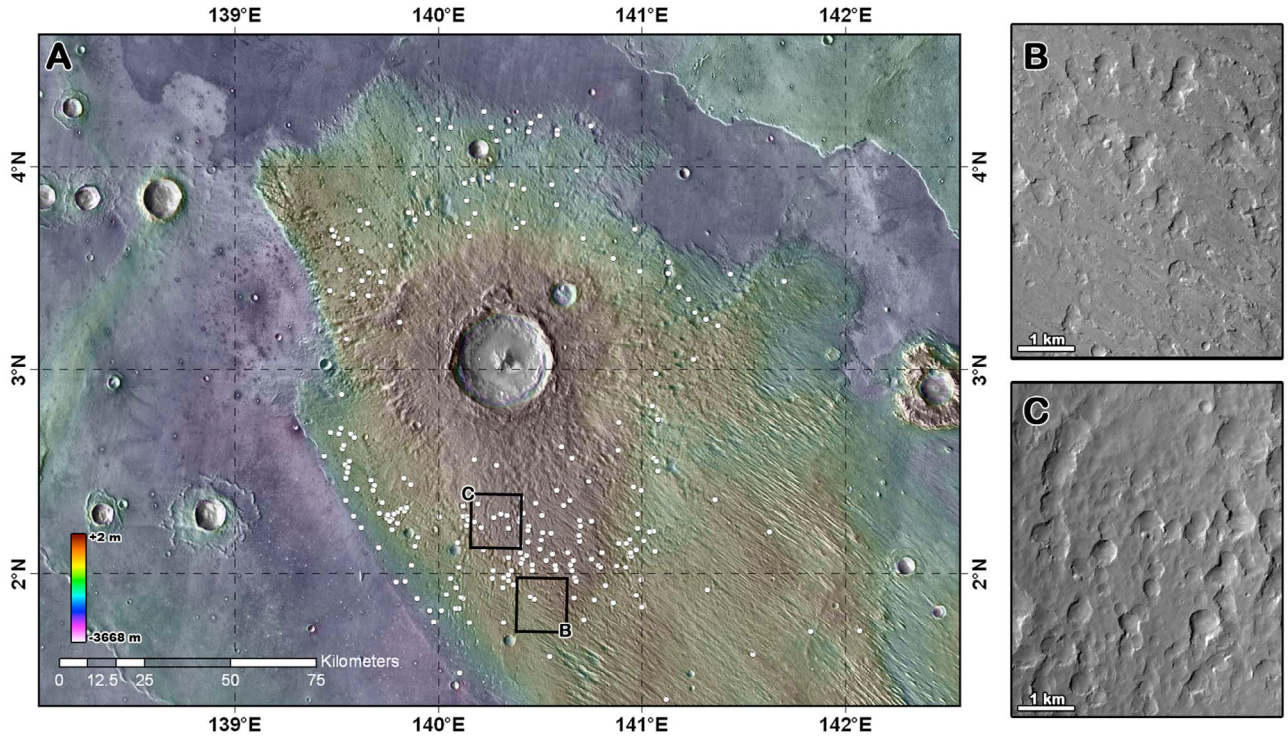

Figure 6. (a) THEMIS mosaic of Crater γ in the Medusae Fossae Formation located at 3.0°N, 140.3°E showing the crater and the surrounding geology for context and secondary craters as white circles. MOLA topography data [*Smith et al.*, 2001] underlies the THEMIS data. (b, c) Close-up panels are CTX data and show some of the secondary crater morphologies observed around this large primary.

the closer secondary craters and so the radial distribution is not illustrated in Figure 5. The size-frequency distribution of the secondaries has a steep −7.8 ± 2.3 slope when fitted $1.5 < D < 2.3$ km (Figure 3c), the second-steepest in this study (Lomonosov was steepest, see Section 3.4).

3.8. Unnamed Crater at 3.0°N, 140.3°E ("Crater γ")

[25] Figure 6 is the unnamed 29.4-km-diameter fresh central peak crater located at 3.0°N, 140.3°E (and named "Crater γ" in this paper). This crater is in northwest Aeolis Planum on one of the western-most parts of the Medusae Fossae Formation (the crater in Section 3.6 is just beyond the eastern part of the Medusae Fossae Formation). This makes it an interesting and unique (in this paper) candidate for study since Medusae Fossae is some of the least dense and friable material on Mars [*Muhleman et al.*, 1991; *Hynek et al.*, 2003]. The crater's continuous ejecta are clear today though it overlies subparallel yardangs of aeolian origin (Figure 6a). The field of secondaries abuts smooth material that has embayed the Medusae Fossae Formation, so these results likely are under-representative of the entire field for this crater. This is preferential toward the north, which may be why fully 70% of the secondary craters identified from this primary are located south of its center. The morphology of these secondary craters is among the more circular type, the secondaries generally being scattered randomly over the continuous ejecta (~1% are beyond the ejecta) and being fairly isolated from each other (Figure 6b). Only a few are in chains (Figure 6c).

[26] 239 craters from the database are probable secondaries from this crater and extend roughly 5.5 crater radii (Table 1). They are all found in a tight annulus of ejecta with the greatest density 2.9 crater radii from the crater's rim (42 km), though azimuthal symmetry was assumed in determining this value, ignoring erosion. The size-frequency distribution of the secondaries has a −5.4 ± 1.9 slope when fitted at $1.7 < D < 2.7$ km (Figure 3e) (5.8–9.2% the primary crater diameter). While these values are typical (see Table 1) despite it being emplaced on Medusae Fossae, this is the second of two cases where the secondaries are all >5% the primary crater diameter (Crater α in Section 3.6 is the other).

3.9. McMurdo Crater

[27] The central peak 24.2-km-diameter McMurdo Crater is the most poleward crater analyzed in this study, located at −84.4°N, 0.5°E. The crater is mostly embedded within the south polar cap, indicating it is fairly young since the south polar cap is estimated to be ~10 Ma [*Herkenhoff and Plaut*, 2000]. Statistically, a ~25-km-diameter crater should form on Mars once every ~4 Ma [*Ivanov*, 2001; *Neukum et al.*, 2001], and taken with the polar cap age constraint means McMurdo may be the youngest ~25-km-diameter crater on Mars. It has a fairly extensive secondary crater field that remains on the cap, though none are visible in the non-ice-covered terrain toward the north indicating resurfacing.

[28] Identifying these secondary craters was initially accomplished in THEMIS Daytime IR mosaics to establish the

phenomenon, but the THEMIS data are inadequate for a study similar to those presented in previous subsections. It is covered fully by CTX imagery; a mosaic was created with fourteen CTX images that cover the field, and it was rendered at 10 m/pix scale. Even with CTX data, identifying the craters was made difficult by both long-term and seasonal erosion processes that dominate the ice cap itself. Nonetheless, the data gathered is in general agreement with the secondary crater fields described for the other primary craters in this study.

[29] 217 craters were identified that are probable secondaries from McMurdo that extend up to ~6 crater radii from the rim (Table 1). They are found scattered in the vicinity of the crater on the remnant ice cap with the greatest density 3.4 crater radii from the rim (82 km), though azimuthal symmetry was assumed in determining this value, ignoring erosion. Fitting the size-frequency distribution between 1.1 and 2.1 km (up to 8.6% the primary crater diameter) yields a -5.2 ± 1.4 slope (Figure 3e).

3.10. Unnamed Crater at 61.7°N, 229.0°E ("Crater δ")

[30] While the crater discussed in Section 3.6 is fairly unique both in this study and on Mars, the unnamed fresh 19.3-km-diameter crater at 61.7°N, 229.0°E displays a similar morphology with long, isolated chains of secondary craters from the primary. However, in this case they are highly linear. It is also surrounded by a double-layer ejecta blanket – the only one in this study, but potentially similar in origin to the single-layer ejecta surrounding Crater β. This crater's nearby secondary field exclusively contains craters that are below the THEMIS resolution for identification. The field is ~75% covered as of January 2011 by public CTX imagery, and eleven CTX images that cover the field were mosaicked at 7.5 m/pix scale.

[31] 1915 craters were identified based on morphology from the CTX imagery that are probable secondaries and extend up to ~10 crater radii from the rim (the most distant of any in this study, though potentially due to the higher resolution data) (Table 1). They are all found predominantly in long chains, but there is a background scattering of secondary craters between the chains - similar to the field from Crater β. The craters were found mainly to the northwest of the primary, possibly indicating an impact direction coming from the southeast or preferential erosion in the southeast. When binned based upon distance from the primary, the greatest density is found 5.5 crater radii from the rim (106 km), the most distant in this study. The size-frequency distribution of the secondaries has a -6.6 ± 1.0 slope when fitted at $0.4 < D < 0.8$ km (Figure 3e); this is fairly steep and could bolster our hypothesis of the reason for Lomonosov's steep distribution, or it could be due to the smaller craters examined.

4. Implications

[32] Detailed studies of known, clear secondary crater fields are important so that their properties can be extrapolated to the broader study of the possible background contamination by secondary craters of planetary surfaces [*McEwen and Bierhaus*, 2006]. From the study of 24 of these fields surrounding Mars primary craters, we find three primary implications.

[33] First, the size-frequency distributions of the secondary craters varied with no noticeable size-dependent pattern. A weighted mean of the slopes is −4.99, which is in general agreement with previous modeling and results [*Bierhaus et al.*, 2005; *McEwen et al.*, 2005; *McEwen and Bierhaus*, 2006], though slightly steeper on average. As with those previous studies, we found a distinct spread in values, being as shallow as −3.3 but as steep as −8.0. All of these are steeper than −3, the asteroidal production function on an incremental SFD [*Ivanov*, 2001; *Neukum et al.*, 2001], and −2, the saturation limit on a cumulative SFD [*Melosh*, 1989]. CTX comparisons show that THEMIS results are reliable for complete identification of secondary fields at these diameters [i.e., *Robbins and Hynek*, 2011]. Thus, the secondary crater production function follows a steep slope overall, but individual craters should be treated as unique events with their own population distribution of secondaries. We posit the two dominant variables in determining the size-frequency distribution are likely to be the initial impactor's velocity and the target material's strength. The impactor velocity is directly proportional to the energy imparted and subsequent shock effects, while the target's strength will determine how it fractures and hence the size-distribution of material for secondary impacts. If this is the case, as future modeling or experiments may demonstrate, then nearby secondary crater populations could be used as a proxy for target strength and/or impactor velocity.

[34] To this end, we separated the primary craters by terrain type (Table 1). Although we are dealing with small numbers – $N = 2$ for each the northern plains, pole/polar, and Medusae Fossae Formation, $N = 4$ on volcanic terrain, and $N = 12$ in the southern highlands – there are some suggestions of trends. The first is that the shallowest SFD slope was for the pole/polar craters with a weighted mean of −4.1. The steepest slopes were found in the northern plains and volcanic terrain with a weighted mean of −6.2. While these are suggestive and support our hypothesis, more examples are needed to determine if these are robust differences and properly characterized. For example, these are also consistent with a potential preservational bias where the slopes decrease over time due to erosion and modification making it more difficult to identify smaller craters.

[35] A second main implication of this work is we found the secondary craters generally followed a Gaussian distribution in number density radial to the primary crater (note that this is a simple radial distribution and we averaged over azimuth regardless of resurfacing to measure it). Though we studied only 24 primary craters, they ranged in diameter from 19 to 222 km and the relative mean distance from the primary was not found to be dependent upon primary crater diameter (in units of primary crater diameter). This distribution had $\mu = 2.44$ crater radii, or 2.37 with the outlier from section 3.9 excluded; the median is 2.32 crater radii from the primary's rim. The mean standard deviation is ±0.87 crater radii, and while it ranged between 0.54 and 1.36 (Table 1), this was also independent of primary crater diameter and independent of the mean of the distribution (except the maximum value outlier from section 3.10). When examining terrain type dependence, we found that craters were closest to their primary (smallest Gaussian mean) in the southern highlands, where the weighted $\mu = 2.2$; pole/polar and volcanic terrain was the most extensive at a weighted $\mu = 3.3$.

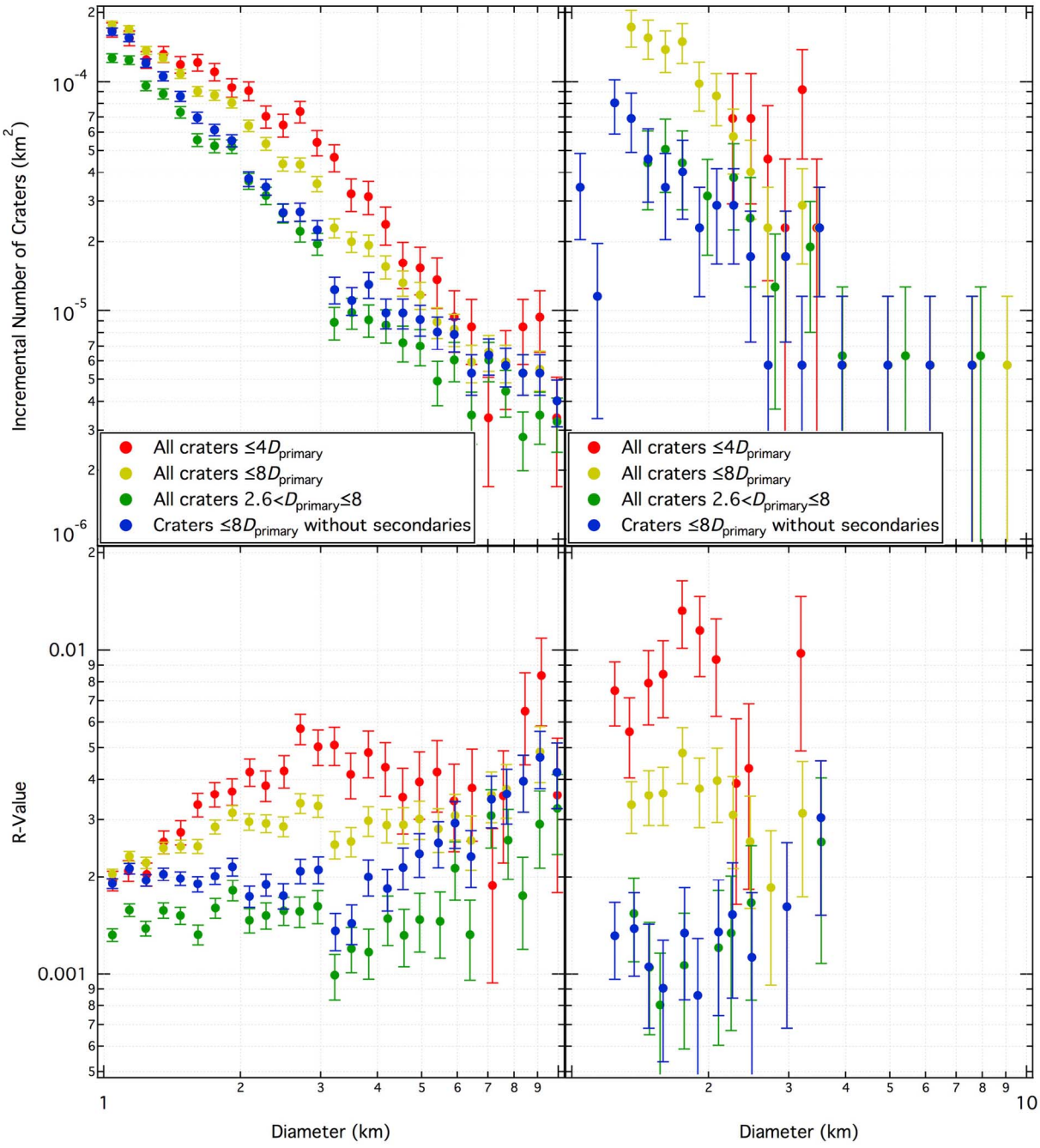

Figure 7. Examples of secondary crater contamination of primary impact craters for two examples, (left) Holden Crater and (right) Crater γ, shown in both (top) incremental SFDs and (bottom) R-plots. Overplotted in color, coded the same in all four panels, are all craters out to distances of 4 crater diameters from the primary in red, 8 diameters in yellow, between 2.6 diameters and 8 diameters in green, and 8 diameters with the selected secondary craters removed in blue. No craters within the primary crater floors are included. From these, it is clear that adjacent secondary crater populations can significantly influence observed crater densities to ranges of at least 8 primary crater radii.

[36] To further explore this Gaussian distribution, we re-examined a field of secondary craters initially identified by *Robbins et al.* [2011]. This field surrounds the D = 5.2 km crater at 5.2°N, 174.6°E, and it is located within the primary caldera of Apollinaris Mons. Even with CTX imagery, it was difficult to morphologically distinguish the small secondary craters around this primary, but we identified a field based upon the over-density of craters around said primary. We have taken the 10,746 small craters identified throughout the Apollinaris Mons caldera and analyzed them for distance from the primary. Even though this includes all craters, there is a noticeable spike well above the background at a mean of 2.4 crater radii from the primary's rim.

This suggests that this pattern holds over a large range of primary crater sizes, at least $5 < D < 222$ km.

[37] Hence, the third main result is that, to avoid nearby secondary crater contamination from automated crater extraction methods from a database, one could reliably exclude 95% of all secondary craters by not using any craters with $D < 0.05D_{primary}$ within 4.2 primary crater radii of the rim (or, more easily for automated methods, within 2.6 crater diameters of the primary crater's center). We do acknowledge that a certain number of primary craters will be excluded in this method, but if one is counting a large area (e.g., equivalent to 8 crater diameters from the primary – see below), then the fraction eliminated is roughly 10%. Any craters actually within the primary crater cannot be simple secondaries from it, so those could be included in counts.

[38] With this in mind, we can take a broader overview of the influence that secondary craters have on local crater statistics and what this means if researchers are not careful in separating secondary craters from primary impact events when deriving stratigraphy and crater-based ages. *McEwen and Bierhaus* [2006] suggest that the majority of craters $D < 1$ km on Mars may be secondaries. While this work cannot address this issue globally but future work from our global database may, we can address the question of local crater population contamination. For example, one can look at the large Holden Crater out to 4 crater diameters from its center (Figure 7, left). As expected based upon the above analysis, the incremental SFD is steeper than would be expected if solely composed of primary craters; it is −3.5 for craters around the ~2–5 km diameter range (~1–3% the primary's diameter, from which the slope was fit in Section 3.3 and Table 1). If we expand this area to 8 crater diameters, which covers 4.7×10^6 km^3 (3.3% the surface area of Mars), there is less of an effect to the point one may think it is a typical production slope of −3.1. However, if the craters within 2.6 diameters of the center are removed, as suggested above, then the slope is −2.8. Finally, the ideal solution is to remove secondary craters by identifying them individually. The SFD looks similar, but there are some minor differences (and the slope over that range is −2.4); regardless of these differences, the removal within 2.6 diameters is a better match to the customized secondary crater removal than the other two examples. On the R-plot, these are the only two that show the relatively flat expected slope between ~1 and 5 km. This also alters the fitted age on the order of 10^8 years, or ~10%, when using the Neukum production function [*Neukum et al.*, 2001].

[39] This analysis was repeated for a smaller, 29.4-km-diameter Crater γ (Section 3.8), in Figure 7, right, with similar conclusions though somewhat different results. The slopes were -6.4 ± 0.7, -5.1 ± 0.3, -1.7 ± 1.4, and -4.5 ± 1.2, respectively. This was a primary crater emplaced on relatively young terrain, Amazonian-aged, as opposed to Holden which is itself significantly older and emplaced on more heavily cratered terrain. Hence, in this crater's case, the population of secondaries from this single event will dominate the statistics to a larger radius. Statistically, the first three population tests shown for this crater are unique, while the detailed removal of secondary craters test yields a more ambiguous result; this is due to there simply being fewer craters: With Holden in this fourth test, there were 8974 craters, whereas this one has 126. While the fits are not as conclusive, examining the data (Figure 7, right) shows the same pattern as with Holden: The simple removal of craters to $2.6D_{primary}$ is the best match to the detailed removal based on individual crater morphology. In fitted ages over a ~1–4 km range, the difference is 800 Ma, or ~25%.

[40] This test was repeated for three more craters from this study (Ritchy, Nier, and Crater ε (see Table 1)), all with similar results where the slope was over-estimated until craters were removed with the closest match to the manual identification being the $2.6D_{primary}$ radius removed, though results were mixed as to how well it mimicked the behavior of manual secondary crater identification. This strongly supports the idea that secondary craters can easily dominate local crater statistics even above a $D = 1$ km proposed transitional diameter, though one can generally eliminate the bulk of contamination by following the steps outlined above.

[41] A caveat with this is when examining more localized crater statistics, especially on young terrain. For example, the largest secondary crater identified around the 19.3-km-diameter primary Crater δ was 1.0 km, 5.2% the primary, but there are numerous ~1-km-diameter *primary* craters within the 200-km radius field of secondary craters, and within the 50-km-radius field of suggested avoidance from the technique above. However, this surface area is ~9,000 km^2, a relatively small region to use $D \sim 1$ km craters for impact statistics - especially on such young terrain - and one that is quite clearly dominated by a relatively large primary. In an alternate case, *Preblich et al.* [2007] showed that Zunil crater's secondary field did not begin until ~16 crater radii from the rim, which is completely outside our suggested region (though these were for "distant" secondary craters entrained within far-reaching rays as opposed to the "nearby" craters we focused on here). Hence, the above-proposed method we think is likely to be generally useful as a rough estimate, and it may be quite accurate in many cases. However, as with any technique, there are instances where it should not be used, such as where there is a clear case of secondary craters not behaving as they do in the cases found in this study, or where there are poor crater statistics to begin with.

5. Conclusions

[42] As we have shown in this study, the secondary craters surrounding larger primary craters generally possess at least one characteristic of classic secondary crater morphology, be it entrainment in troughs or tendrils radial to the primary, highly asymmetric, biaxially symmetric with the symmetry axis radial to the primary, or immediately surrounded by herring-bone ejecta that points back to the primary (Figure 2); we were unable to explore depth versus diameter relationships due to insufficient topographic resolution (secondaries should be shallower than primaries of the same size due to lower impact velocity [e.g., *Melosh*, 1989; *McEwen and Bierhaus*, 2006]). While these features have all been known of for decades, the sheer range of different morphologies expressed deserves more discussion. In this work and our related work toward a large, global crater database [*Robbins*, 2011], the single-crater-wide chains and tendrils of secondaries isolated from little to no background field were only observed around craters with LE-type ejecta (e.g., Figure 5). Where lunar-type radial ejecta were present, secondary cra-

ters were observed embedded in troughs within it (e.g., Figures 2a and 6). Meanwhile, even around older craters (such as Holden or Crater α), where secondary craters were degraded, they were still generally distinguishable by non-circular shapes with a long axis oriented radial to the primary (e.g., Figures 2c, 4, 5, and 6).

[43] From the analyses presented here, we can conclude: (1) Each primary impact event can produce a distinct size-frequency distribution of secondary craters that, when taken as a whole, have a canonical slope between −4.0 and −6.0, but individually can be significantly different, and (2) our results suggest there is a terrain dependence on the size-frequency distribution of secondary crater populations. (3) Secondary crater spatial densities close to their primary tend to follow a Gaussian distribution in number versus distance from the primary, and the mean peak spatial density of that distribution is 2.6 crater diameters from the primary's center. This is a pattern that holds over at least 1.6 orders of magnitude of crater diameters (~5 < D < ~220 km). This can be used in automated crater counting to eliminate these craters to avoid the majority of secondary crater contamination. (4) Local and regional crater populations can be significantly contaminated by secondary craters over a large surface area; Holden Crater's secondary craters will still affect size-frequency distributions over a surface area >3% of Mars' surface.

[44] (5) The *local* onset of this contamination may be several times the D = 1 km suggested by *McEwen and Bierhaus* [2006] for a global Martian crater population, and so even at multikilometer sizes, researchers must take care to avoid secondary crater contamination when using craters for age-dating purposes. For example, the secondary craters produced from just 30 Holden-sized and -type events evenly distributed around the globe would contaminate the crater population D < 5 km across the entire planet; the global crater database used in this study shows there are 95 such impacts (although they are not evenly distributed in time nor space) [*Robbins*, 2011]. This is in stark contrast with recent work that suggests the contrary [e.g., *Neukum et al.*, 2001, 2006; *Hartmann*, 2007]. However, a caveat to this is that the two main populations of secondary craters – nearby (this study) and distant (other studies such as those of *Bierhaus et al.* [2005], *McEwen et al.* [2005], *Preblich et al.* [2007], and *Robbins and Hynek* [2011]) – may represent two different formation mechanisms, and hence the statistics presented may not be as valid to the general "background secondary" population.

[45] Additional implications of this work not discussed in-depth in Section 4 include: (6) In a few cases, the field of secondary craters can be larger than the hypothesized maximum 5% of the primary crater's diameter (see Sections 3.6 and 3.8 and Figure 4). (7) Nearby secondary crater fields appearing in thin tendrils or chains were only found around craters with cohesive layered ejecta (LE) -type morphology, implying a possible formation-dependent link. (8) The LE-type ejecta morphology craters also had SFD slopes significantly steeper than the collective mean from all craters studied here. Though this may be attributed to the terrain- or preservation-dependent nature in slope addressed above, work suggests the LE ejecta formation is also terrain dependent [e.g., *Barlow*, 2006; *Robbins*, 2011]. Hence, separating these two possible effects may be secondary and difficult to accomplish in future endeavors. Similarly, (9) Lomonosov's SFD slope presents an outlier that may be explained by a near-surface cryosphere, but we were unable to test this hypothesis because the only other high-northern latitude crater examined was a layered ejecta crater.

[46] Further research into these issues and separating each potential dependent variable's effect from the others is important to understand how to account for secondary craters when primary craters are the feature of importance. Our global crater database [*Robbins*, 2011] will contain a classification of whether a crater is a probable secondary and from which primary it originated if this can be determined, but this is only for morphologically clear secondary impacts. Degraded primary craters may look identical to a secondary at that location $5D_{primary}$ from a large primary crater, especially at the kilometer scale when using 100 m/pix mosaics. This problem must be better understood as a function of terrain as well, since this study and others [e.g., *McEwen and Bierhaus*, 2006] show there may be terrain dependence upon secondary field characteristics. Examination of secondary crater fields and production on other surfaces (e.g., with Lunar Reconnaissance Orbiter imagery of the Moon and MESSENGER imagery on Mercury) may help further constrain this issue to better model their production so they can be taken into account in a statistical and automated manner without needing to examine the morphology of every crater. However, such a model will also be incomplete without a better understanding of secondary craters produced very far from their primary [e.g., *Bierhaus et al.*, 2005; *McEwen et al.*, 2005; *Robbins and Hynek*, 2011], which this study did not investigate. Overall, a more robust framework and understanding of secondary cratering is needed to better constrain planetary surface ages and their implications for the overall history of the solar system.

[47] **Acknowledgments.** The authors thank E. B. Bierhaus and I. Daubar for their helpful reviews. S. J. Robbins thanks his dissertation committee, especially N. G. Barlow, for additional feedback used to improve this work. Support for this work was through NASA Award NNX10AL65G.

References

Arvidson, R., et al. (1979), Standard techniques for presentation and analysis of crater size-frequency data, *Icarus*, *37*, 467–474, doi:10.1016/0019-1035(79)90009-5.

Barlow, N. G. (2006), Impact craters in the northern hemisphere of Mars: Layered ejecta and central pit characteristics, *Meteorit. Planet. Sci.*, *41*(10), 1425–1436, doi:10.1111/j.1945-5100.2006.tb00427.x.

Barlow, N. G., J. M. Boyce, F. M. Costard, R. A. Craddock, J. B. Garvin, S. E. H. Sakimoto, R. O. Kuzmin, D. J. Roddy, and L. A. Soderblom (2000), Standardizing the nomenclature of Martian impact crater ejecta morphologies, *J. Geophys. Res.*, *105*(E11), 26,733–26,738, doi:10.1029/2000JE001258.

Bierhaus, E. B., C. R. Chapman, and W. J. Merline (2005), Secondary craters on Europa and implications for cratered surfaces, *Nature*, *437*, 1125–1127, doi:10.1038/nature04069.

Boynton, W. V., et al. (2002), Distribution of hydrogen in the near surface of Mars: Evidence for subsurface ice deposits, *Science*, *297*, 81–85, doi:10.1126/science.1073722.

Chapman, C. R., and R. R. Haefner (1967), A critique of methods for analysis of the diameter-frequency relation for craters with special application to the Moon, *J. Geophys. Res.*, *72*(2), 549–557, doi:10.1029/JZ072i002p00549.

Christensen, P. R., et al. (2004), The Thermal Emission Imaging System (THEMIS) for the Mars 2001 Odyssey Mission, *Space Sci. Rev.*, *110*(1), 85–130, doi:10.1023/B:SPAC.0000021008.16305.94.

Dickson, J. L., C. I. Fassett, and J. W. Head (2009), Amazonian-aged fluvial valley systems in a climatic microenvironment on Mars: Melting of

ice deposits on the interior of Lyot Crater, *Geophys. Res. Lett.*, *36*, L08201, doi:10.1029/2009GL037472.
Golombek, M., et al. (2010), Landing sites under consideration for Mars Science Laboratory, *Lunar Planet. Sci.*, *XLI*, Abstract 2407.
Grant, J. A., R. P. Irwin III, J. P. Grotzinger, R. E. Milliken, L. L. Tornabene, A. S. McEwen, C. M. Weitz, S. W. Squyres, T. D. Glotch, and B. J. Thomson (2008), HiRISE imaging of impact megabreccia and sub-meter aqueous strata in Holden Crater, *Mars, Geology*, *36*(3), 195–198, doi:10.1130/G24340A.1.
Hartmann, W. K. (2005), Martian cratering 8: Isochron refinement and the chronology of Mars, *Icarus*, *174*, 294–320, doi:10.1016/j.icarus.2004.11.023.
Hartmann, W. K. (2007), Martian cratering 9: Toward resolution of the controversy about small craters, *Icarus*, *189*, 274–278, doi:10.1016/j.icarus.2007.02.011.
Herkenhoff, K. E., and J. J. Plaut (2000), Surface ages and resurfacing rates of the polar layered deposits on Mars, *Icarus*, *144*, 243–253, doi:10.1006/icar.1999.6287.
Hynek, B. M., R. J. Philips, and R. E. Arvidson (2003), Explosive volcanism in the Tharsis region: Global evidence in the Martian geologic record, *J. Geophys. Res.*, *108*(E9), 5111, doi:10.1029/2003JE002062.
Ivanov, B.A. (2001), Mars/Moon cratering rate ratio estimates, *Chronol. Evol. Mars*, *96*, 87–104.
Lucchitta, B. K. (1977), Crater clusters and light mantle at the Apollo 17 site; A result of secondary impacts from Tycho, *Icarus*, *30*, 80–96, doi:10.1016/0019-1035(77)90123-3.
Malin, M. C., et al. (2007), Context Camera investigation on board the Mars Reconnaissance Orbiter, *J. Geophys. Res.*, *112*, E05S04, doi:10.1029/2006JE002808.
McEwen, A. S., and E. B. Bierhaus (2006), The importance of secondary cratering to age constraints on planetary surfaces, *Annu. Rev. Earth Planet. Sci.*, *34*, 535–567, doi:10.1146/annurev.earth.34.031405.125018.
McEwen, A. S., B. S. Preblich, E. P. Turtle, N. A. Artemieva, M. P. Golombek, M. Hurst, R. L. Kirk, D. M. Burr, and P. R. Christensen (2005), The rayed crater Zunil and interpretations of small impact craters on Mars, *Icarus*, *176*, 351–381, doi:10.1016/j.icarus.2005.02.009.
Melosh, H. J. (1989), *Impact Cratering: A Geologic Process*, Oxford Univ. Press, New York.
Muhleman, D. O., B. J. Butler, A. W. Grossman, and M. A. Slade (1991), Radar images of Mars, *Science*, *253*, 1508–1513, doi:10.1126/science.253.5027.1508.
Neukum, G., B. A. Ivanov, and W. K. Hartmann (2001), Cratering records in the inner solar system in relation to the lunar reference system, *Chronol. Evol. Mars*, *96*, 55–86.
Neukum, G., S. C. Werner, and B. A. Ivanov (2006), The characteristics of the impact crater production size-frequency distributions on the solar system planetary bodies, their relationships to asteroidal and cometary impacts, and the question of secondary-cratering contributions, Abstract 6005 presented at Workshop on Surface Ages and Histories: Issues in Planetary Chronology, Lunar Planet. Inst., Houston, Tex., 21–23 May.
Oberbeck, V. R., and R. H. Morrison (1974), Laboratory simulation of the herringbone pattern associated with lunar secondary crater chains, *Moon*, *9*, 415–455, doi:10.1007/BF00562581.
Preblich, B. S., A. S. McEwen, and D. M. Studer (2007), Mapping rays and secondary craters from the Martian crater Zunil, *J. Geophys. Res.*, *112*, E05006, doi:10.1029/2006JE002817.
Robbins, S. J. (2011), Surface properties, cratering physics, and the volcanic history of Mars from a new global Martian crater database, Ph.D. thesis, Univ. of Colo., Boulder.
Robbins, S. J., and B. M. Hynek (2011), Distant secondary craters from Lyot Crater, Mars, and implications for surface ages of planetary bodies, *Geophys. Res. Lett.*, *38*, L05201, doi:10.1029/2010GL046450.
Robbins, S. J., G. Di Achille, and B. M. Hynek (2011), The volcanic history of Mars: High-resolution crater-based studies of the calderas of 20 volcanoes, *Icarus*, *211*, 1179–1203, doi:10.1016/j.icarus.2010.11.012.
Schultz, P. H., and J. Singer (1980), A comparison of secondary craters on the Moon, Mercury, and Mars, *Proc. Lunar Planet. Sci. Conf.*, *11*, 2243–2259.
Scott, D. H., and K. L. Tanaka (1986), Geologic map of the western equatorial region of Mars, *U.S. Geol. Surv. Misc. Invest. Map I-1802-A*.
Shoemaker, E. M. (1962), Interpretation of lunar craters, in *Physics and Astronomy of the Moon*, edited by Z. Kopal, pp. 283–359, Academic, New York.
Shoemaker, E. M. (1965), Preliminary analysis of the fine structure of the lunar surface in Mare Cognitum, in *The Nature of the Lunar Surface*, edited by W.N. Heiss, D.R. Menzel, and J.A. O'Keefe, pp. 23–77, Johns Hopkins Univ. Press, Baltimore, Md.
Smith, D. E., et al. (2001), Mars Orbiter Laser Altimeter: Experiment summary after the first year of global mapping of Mars, *J. Geophys. Res.*, *106*(E10), 23,689–23,722, doi:10.1029/2000JE001364.
Tanaka, K. L. (1986), The stratigraphy of Mars, *J. Geophys. Res.*, *91*(B13), E139–E158, doi:10.1029/JB091iB13p0E139.
Tanaka, K. L., J. A. Skinner Jr., and T. M. Hare (2005), Geologic map of the northern plains of Mars, *U.S. Geol. Surv. Misc. Invest. Map I-2888*.
Tanaka, K. L., C. M. Fortezzo, J. M. Dohm, R. P. Irwin III, J. A. Skinner Jr., T. M. Hare, T. Platz, and S. J. Robbins (2011), Completing the new global geologic map of Mars, *Lunar Planet. Sci.*, *XLII*, Abstract 2265.
Thomson, B. J., and J. W. Head III (2001), Utopia Basin, Mars: Characterization of topography and morphology and assessment of the origin and evolution of basin internal structure, *J. Geophys. Res.*, *106*, 23,209–23,230, doi:10.1029/2000JE001355.

B. M. Hynek and S. J. Robbins, Laboratory for Atmospheric and Space Physics, University of Colorado at Boulder, UCB 392, Boulder, CO 80309, USA. (hynek@lasp.colorado.edu; stuart.robbins@colorado.edu)